

Inelastic neutron scattering studies of YFeO_3

S. E. Hahn, A. A. Podlesnyak, G. Ehlers, and G. E. Granroth

Quantum Condensed Matter Division, Oak Ridge National Laboratory, Oak Ridge, Tennessee 37831, USA

R. S. Fishman

Materials Science and Technology Division, Oak Ridge National Laboratory, Oak Ridge, Tennessee 37831, USA

A. I. Kolesnikov

Chemical and Engineering Materials Division, Oak Ridge National Laboratory, Oak Ridge, Tennessee 37831, USA

E. Pomjakushina and K. Conder

Laboratory for Developments and Methods, Paul Scherrer Institut, CH-5232, Villigen-PSI, Switzerland

(Received 11 September 2013; revised manuscript received 20 December 2013; published 23 January 2014)

Spin waves in the rare-earth orthoferrite YFeO_3 have been studied by inelastic neutron scattering and analyzed with a full four-sublattice model including contributions from both the weak ferromagnetic and antiferromagnetic orders. Antiferromagnetic exchange interactions of $J_1 = -4.23 \pm 0.08$ (nearest neighbors only) or $J_1 = -4.77 \pm 0.08$ meV and $J_2 = -0.21 \pm 0.04$ meV lead to excellent fits for most branches at both low and high energies. An additional branch associated with the weak antiferromagnetic order was observed. This work paves the way for studies of other materials in this class containing spin reorientation transitions and magnetic rare-earth ions.

DOI: [10.1103/PhysRevB.89.014420](https://doi.org/10.1103/PhysRevB.89.014420)

PACS number(s): 78.70.Nx, 75.30.Ds, 75.10.Hk, 75.25.-j

I. INTRODUCTION

The rare-earth orthoferrites $R\text{FeO}_3$ are an important family of materials whose magnetic properties remain a focus of considerable research due to promising applications in innovative spintronic devices [1]. Furthermore, they contribute to an emerging class of materials, i.e., multiferroics with strong magnetoelectric (ME) coupling [2,3]. In multiferroic materials, the coupling between magnetic and ferroelectric order gives rise to magnetization on the application of an electric field or to electric polarization on the application of a magnetic field. Their complex noncollinear structures and magnetic phase transitions are due to the combination of the antiferromagnetic (AFM) exchange interaction with the Dzyaloshinsky-Moriya (DM) antisymmetric exchange interaction [4,5].

In general materials in the $R\text{FeO}_3$ family contain two magnetic subsystems consisting of either iron or rare-earth ions. With decreasing temperature or an applied magnetic field, most of these materials undergo a spin reorientation transition from $\Gamma_4(G_a, F_c)$, where the net moment is along the c axis, to $\Gamma_2(G_c, F_a)$, where the net moment is along the a axis (for notation, see Appendix A) [6]. This transition occurs over a finite temperature range where the spins rotate continuously in the lower symmetry phase $\Gamma_{24}(G_{ac}, F_{ca})$. No structural change is observed in ErFeO_3 and YbFeO_3 , suggesting that this is purely a magnetic transition [7,8]. The rotation of the iron moments leads to a change in the magnitude of the magnetization on the rare-earth subsystem, which must be included in the calculation of the rotation angle and absolute magnetization. At lower temperatures an additional magnetic transition occurs when the rare-earth moments order.

The nonmagnetic yttrium sublattice in YFeO_3 enables us to focus only on the magnetic interactions of the iron sublattices. The lack of a spin reorientation transition with temperature considerably simplifies the modeling of spin

dynamics and makes YFeO_3 a good stepping stone to studying other materials in this class with more complex dynamics.

YFeO_3 adopts an orthorhombic structure with space group $Pbnm$. Below 640 K, YFeO_3 is a noncollinear antiferromagnet whose four Fe^{3+} ions are in the state $\Gamma_4(G_a, F_c, A_b)$, shown in Fig. 1. A dominant antiferromagnetic order occurs along the a axis. A weak ferromagnetic component along the c axis is associated with the spin canting with respect to the ab plane and exists in both models. In the two-sublattice model, the spins (1–3) and (2–4) are equivalent, whereas they become inequivalent in the four-sublattice model. This doubles the periodicity along the c axis, yielding a modulation of the ferromagnetic component along c and a weak antiferromagnetic component along b . The ratio of A_b/G_a , which determines the canting angle along b , was found to be $1.59(7) \times 10^{-2}$ [9]. Values for F_c/G_a range from 8.9×10^{-3} to 1.29×10^{-2} where the lower values may be due to ferromagnetic impurities. These values set limits on the canting angle along c .

Spin waves in similar systems TmFeO_3 and ErFeO_3 were previously measured and modeled with a combination of four-sublattice and two-sublattice models for the short-wavelength and long-wavelength dispersion, respectively [10]. For TmFeO_3 , the exchange constant for nearest neighbors only ($J_2 \equiv 0$) was found to be $J_1 = -4.22$ meV. With next-nearest neighbors included, the exchange constants were $J_1 = -5.02$ meV and $J_2 = -0.324$ meV. A four-sublattice model containing only exchange predicts reasonable energies for the observed spin wave branches. The two easy-axis anisotropy parameters are approximately equal near the transition and an additional term proportional to the fourth power of the spin controls the rotation angle over the temperature range of the transition.

TbFeO_3 has generated renewed interest since measurements in an applied magnetic field found an unusual incommensurate phase with a periodic array of widely separated domain walls. The ordering of domain walls is due to a

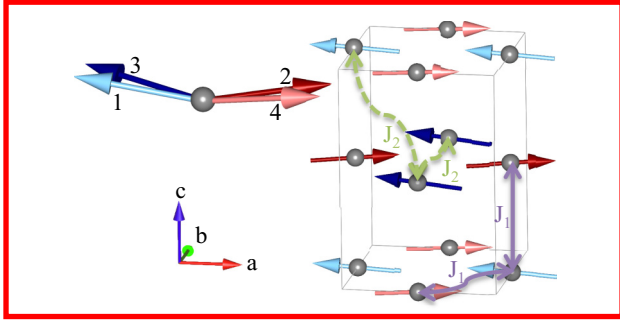


FIG. 1. (Color online) Magnetic unit cell of YFeO_3 , showing only the positions of the Fe^{3+} atoms. The four sublattices show weak ferromagnetism and antiferromagnetism along the c and b directions, respectively. Exchange interactions between nearest (J_1) and next-nearest (J_2) neighbors are shown by the solid purple and dashed green arrows, respectively.

long-range force from the exchange of magnons propagating through the iron sublattice [11]. Spin waves in TbFeO_3 were previously measured and modeled with a four-sublattice model containing only exchange interactions [12]. In principle, the distortion from cubic symmetry leads to different exchange constants for nearest and next-nearest neighbors within the ab plane and between planes. The measured distances between Fe^{3+} ions are, however, within 2% and 6% of each other for nearest neighbors and next-nearest neighbors, respectively. In each of these cases, the exchange parameters within the ab plane and between planes can be treated as equal. With only nearest neighbors, $J_1 = -4.34$ meV and with both nearest and next-nearest neighbors the exchange constants were $J_1 = -4.95$ meV and $J_2 = -0.241$ meV.

In YFeO_3 , spin waves were measured at 1.4 and 2.2 meV in the long-wavelength limit with Raman scattering at room temperature [13]. A two-sublattice model was then used to obtain estimates for the anisotropy constants, defined in Eq. (1), of $K_a = 4.6 \times 10^{-3}$ meV and $K_c = 1.13 \times 10^{-3}$ meV. In this work, we measured spin waves in YFeO_3 by inelastic neutron scattering on two different energy scales and analyzed them simultaneously with a quantitative model considering contributions from both the weak ferromagnetic and antiferromagnetic orders present in the full four-sublattice model.

II. EXPERIMENT

Polycrystalline YFeO_3 was prepared by a solid state reaction. The starting materials of Y_2O_3 and Fe_2O_3 with 99.99% purity were mixed and ground followed by a heat treatment in air at 1000–1250 °C for at least 70 hours with several intermediate grindings. The phase purity of the resulting compound was checked with a conventional x-ray diffractometer. The resulting powder was hydrostatically pressed into rods (8 mm in diameter and 60 mm in length) and subsequently sintered at 1400 °C for 20 hours.

The crystal growth was carried out using an optical floating zone furnace (FZ-T-10000-H-IV-VP-PC, Crystal System Corp., Japan) with four 500 W halogen lamps as heat sources. The growing conditions were as follows: the growth rate was 5 mm/h, the feeding and seeding rods were rotated at about 15 rpm in opposite directions to ensure the liquid's homo-

geneity, and an oxygen and argon mixture at 1.5 bar pressure was applied during growth. The lattice constants in the $Pbnm$ space group were $a = 5.282$ Å, $b = 5.596$ Å, and $c = 7.605$ Å. The sample was orientated in the (HOL) plane for neutron measurements.

Inelastic neutron scattering measurements were done using the Cold Neutron Chopper Spectrometer (CNCS) [14] and the Fine Resolution Chopper Spectrometer (SEQUOIA) [15,16] at the Spallation Neutron Source (SNS) at Oak Ridge National Laboratory. The data were collected using fixed incident neutron energies 99.34 meV (SEQUOIA) and 3.15 meV (CNCS), which allowed for the measurement of excitations up to energy transfers of $\Delta\omega \sim 80$ meV (SEQUOIA) and 2.5 meV (CNCS). In these configurations, a full width at half maximum (FWHM) resolution of 5.5 meV (SEQUOIA) and 0.06 meV (CNCS) was obtained at the elastic position. The sample was cooled to 4 K on SEQUOIA and base temperature (<2 K) on CNCS. The MANTIDPLOT [17] and DAVE [18] software packages were used for data reduction and analysis.

III. THEORETICAL MODELING OF SPIN WAVES

Our model Hamiltonian, given in Eq. (1), contains isotropic exchange constants J_1 and J_2 coupling nearest-neighbor and next-nearest-neighbor Fe^{3+} spins, two DM antisymmetric exchange constants D_1 and D_2 responsible for the canting along c and b and two easy-axis anisotropy constants K_a and K_c along the a and c axes

$$\begin{aligned}
 H = & -J_1 \sum_{\langle i,j \rangle} \mathbf{S}_i \cdot \mathbf{S}_j - J_2 \sum_{\langle i,j' \rangle} \mathbf{S}_i \cdot \mathbf{S}_j \\
 & - D_1 \sum_{\mathbf{R}_j = \mathbf{R}_i + a(\hat{x} \pm \hat{y})} \hat{y} \cdot \mathbf{S}_i \times \mathbf{S}_j \\
 & - D_2 \sum_{\mathbf{R}_j = \mathbf{R}_i + a(\hat{x} \pm \hat{y})} \hat{z} \cdot \mathbf{S}_i \times \mathbf{S}_j \\
 & - K_a \sum_i (S_i^x)^2 - K_c \sum_i (S_i^z)^2. \quad (1)
 \end{aligned}$$

The DM interaction was only considered among nearest neighbors within the ab plane, which is the minimum necessary to explain the canting of all four sublattices. A third DM interaction is possible along b with nearest neighbors between planes, but is not needed to describe the spin structure and would add additional complexity to our model.

Each of the four spins are written in spherical coordinates as

$$\mathbf{S}_i = S(\sin \theta_i \cos \phi_i, \sin \theta_i \sin \phi_i, \cos \theta_i), \quad (2)$$

where $S = 5/2$. The angle θ_i is defined with respect to the c axis. The angle ϕ_i is defined with respect to the a axis when the spin is projected into the ab plane. As a first step in this analysis, one must find the angles associated with the minimum classical energy. By assuming that $\theta_i = \theta$ for all sublattices and $\phi_1 = \pi + \phi$, $\phi_2 = \phi$, $\phi_3 = \pi - \phi$, and $\phi_4 = 2\pi - \phi$, the number of independent angles is reduced to two. Assuming small angles, one can linearize the problem and find the expressions in Eqs. (3) and (4) for θ and ϕ to lowest order

as a function of J_1 , J_2 , D_1 , D_2 , K_a , and K_c

$$\theta = \frac{\pi}{2} + \frac{2D_1}{6J_1 + K_c - K_a}, \quad (3)$$

$$\phi = -\frac{2D_2}{4J_1 - 8J_2 - K_a}. \quad (4)$$

In the above expressions, $\theta \leq \frac{\pi}{2}$ and $\phi > 0$. Next these expressions were then used to find values for D_1 and D_2 that produce the experimentally determined canting angles. The ratio of $F_c/G_a = 1.29 \times 10^{-2}$ and $A_b/G_a = 1.59 \times 10^{-2}$ were used to fix the angles $\theta = 1.5656$ (89.70°) and $\phi = 0.0032$ (0.18°) [9].

The inelastic neutron cross section for undamped spin waves is

$$S(\mathbf{q}, \omega) = \sum_{\alpha, \beta} (\delta_{\alpha\beta} - q_\alpha q_\beta / q^2) S_{\alpha\beta}(\mathbf{q}, \omega) \quad (5)$$

$$= \sum_{n, \alpha} [1 - (q_\alpha / q)^2] \delta(\omega - \omega_n(\mathbf{q})) S_{\alpha\alpha}^{(n)}(\mathbf{q}), \quad (6)$$

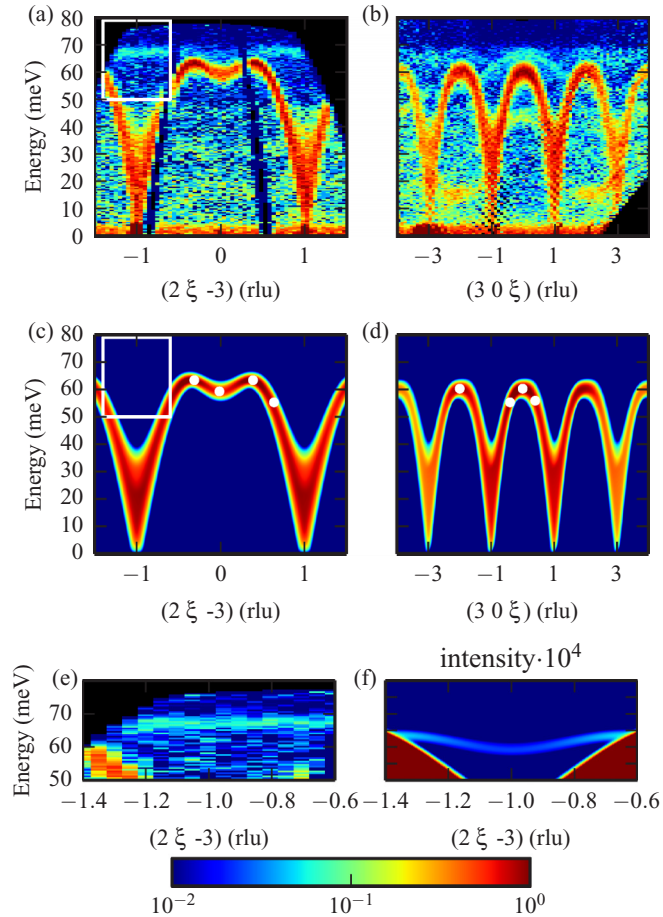


FIG. 2. (Color online) Measured spin wave dispersion along (a) $(2, \xi, -3)$ and (b) $(3, 0, \xi)$ and calculated spin wave dispersion along (c) $(2, \xi, -3)$ and (d) $(3, 0, \xi)$. The background contains phonon modes not included in our model. (e) Enlargement of the region outlined by the white box in (a). (f) Enlargement on the region outlined by the white box in (c) and with the intensity multiplied by 10^4 . In all figures, the white dots show energies used for fitting. Black pixels show regions where no data were collected.

where α and β are the Cartesian directions x, y, z and n enumerates the individual branches [19]. $S_{\alpha\beta}(\mathbf{q}, \omega)$ is the spin-spin correlation function describing undamped spin waves at low temperature. The spin-spin correlation function is diagonal when there is no net moment and antisymmetric otherwise, meaning that off-diagonal elements do not contribute to the intensity. The energies $\omega_n(\mathbf{q})$ and terms contributing to the scattering intensities $S_{\alpha\alpha}^{(n)}(\mathbf{q})$ were solved using the $1/S$ formalism outlined in Ref. [20] and Appendix A of Ref. [21]. For direct comparison to experimental intensities, the effects of the magnetic form factor, instrumental resolution function, and integration width were included in our calculations according to Appendix B.

To find the set of parameters that best fits the data, the energy with the highest intensity was taken at eight points in reciprocal space that described the shape of the spin wave dispersion. Our model finds two branches with similar energies contributing to the highest intensity branch. The energy differences range from 0.8 meV at the zone center to 0.01 meV at the zone boundary. These branches are, however, too close in energy to be resolved separately in the cuts shown in Figs. 2(c) and 2(d), so the energy bin with the highest intensity was compared against the average of the two energies weighted by their intensities.

At the zone center we used the observed energies from Ref. [13] of 1.4 and 2.2 meV. The lower value is in good agreement with measurements from CNCS shown in Fig. 3, though we were not able to independently verify the frequency of the second mode. The variance was estimated by a Gaussian fit to the measured data. The exchange and anisotropy parameters J_1, J_2, K_a , and K_c were fitting parameters, D_1 and D_2 were adjusted for each calculation using Eq. (3), and the canting angles θ in ϕ remained fixed. The NLOPT nonlinear-optimization package [22] was used for the least-squares fitting. Error bars indicate when the reduced χ^2 increases by 1.0. For D_1 and D_2 we propagated the error assuming a 10% error in the canting angles.

The parameters determined from this fit along with data from similar work on YFeO₃ and similar materials is given in Table I. The values for J_1 are considerably lower than

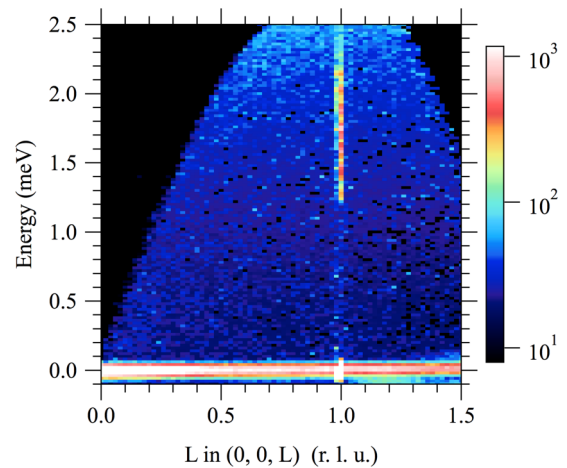


FIG. 3. (Color online) Spin wave energy gap in YFeO₃ measured by inelastic neutron scattering.

TABLE I. Best fit parameters used in this work and compared to other work on YFeO_3 and similar materials. In the second line only nearest neighbors were included ($J_2 = 0.0$). All values are in meV.

Material	Num. SL	J_1	J_2	D_1	D_2	K_a	K_c
YFeO_3	4	-4.77 ± 0.08	-0.21 ± 0.04	0.074 ± 0.008	0.028 ± 0.003	0.0055 ± 0.0002	0.00305 ± 0.0002
	4	-4.23 ± 0.08	0.0	0.066 ± 0.007	0.028 ± 0.003	0.0063 ± 0.0002	0.0036 ± 0.0002
YFeO_3 Ref. [13]	2	-4.96	0.0	0.11		0.0046	0.0011
TmFeO_3 Ref. [10]	4	-5.01	-0.32				
	4	-4.22	0.0				
TbFeO_3 Ref. [12]	4	-4.94	-0.24				
	4	-4.34	0.0				

those published by White *et al.*, possibly because their fit considered only the long wavelength limit. Our results are similar to those of Shapiro *et al.* [10] and Gukasov *et al.* [12] in similar materials. Anisotropy parameters are not equal in the two-sublattice and four-sublattice models because the weak antiferromagnetic order is absorbed into renormalized anisotropy parameters [23]. Therefore anisotropy parameters should not be directly compared between two and four sublattice models.

IV. DISCUSSION

Overall, excellent fits are obtained for most branches. Figures 2(a) and 2(c) show the measured and calculated spin wave dispersion along $(2, \xi, -3)$. Both show a dip in frequency and intensity at $(2, 0, -3)$ and the integration range and experimental resolution explain the line width. The intensity around 70 meV near $\xi = -1, 1$ appears to be magnetic scattering and is not visible in our calculation on this intensity scale. Figure 2(e) enlarges the region in Fig. 2(a) near $\xi = -1$ outlined by the white box. Spin wave branches in this region are also reported elsewhere [10,12]. The two-sublattice model does not contain any branches near $\xi = -1, 1$ that could explain this intensity. Two-magnon scattering occurs around 120 meV, well above the range of energy transfers we measured [24]. A full four-sublattice model doubles the unit cell, leading to zone folding and consequently two additional branches close to those energies. The weak antiferromagnetic order gives these additional branches some intensity, motivating us to model this system with the full four-sublattice model.

When $\phi = 0$ this branch has zero intensity, consistent with zone folding in a supercell. A nonzero value of ϕ makes sublattices 1,3 and 2,4 unequal and gives this branch some intensity. Figure 2(f) shows this same region in our calculation, though with the intensity multiplied by 10^5 . At these small angles, changing D_2 , and consequently the ϕ angle, has the greatest effect on the intensity of this branch whereas chaining D_1 , or the θ angle, has little if any effect. The ratio of the intensities of these two branches is more than four orders of magnitude too weak compared to the measured ratio of 0.07. Small changes in these angles alone are not enough to account for this difference. In addition, measured energies are up to 9 meV higher than what would be expected from zone folding. Quantum fluctuations are missing from this model and may have an effect on these energies and intensities.

Agreement remains excellent along other directions. Figures 2(b) and 2(d) show the calculated and measured spin wave dispersion along $(3, 0, \xi)$. The calculated energies agree well with the measured values. The integration range and resolution function accounts for the observed widths, especially at low energies. Aluminum and phonon scattering have not been subtracted and may account for any structure seen in the background.

To show how the spin wave intensities depend on the location in reciprocal space, Figs. 4(a) and 4(c) show the calculated and observed spin wave dispersion along $(2, \xi, -2)$. Despite identical energies, the intensity is dramatically different from that observed along $(2, \xi, -3)$ in Fig. 2. Along $(2, \xi, -2)$ the intensity approaches the background at low

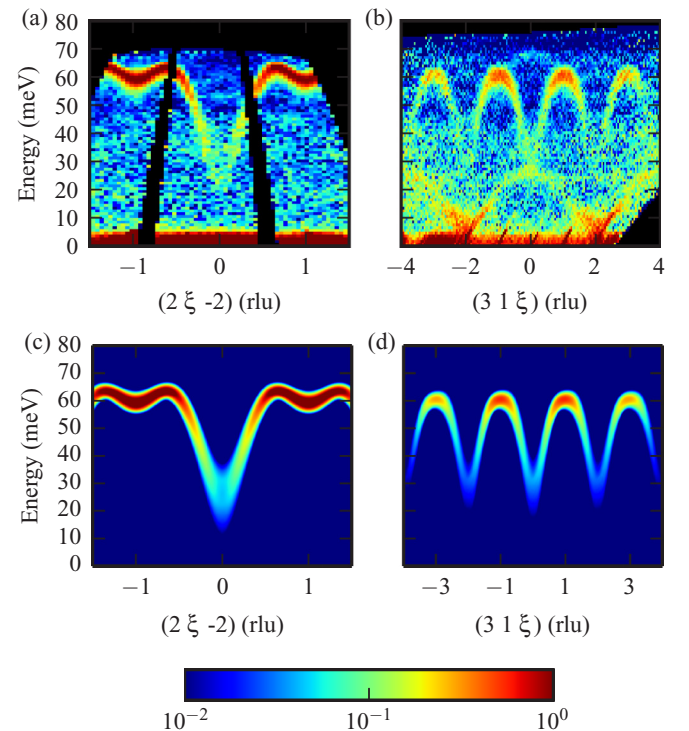


FIG. 4. (Color online) (a) Measured spin wave dispersion along (a) $(2, \xi, -2)$ and (b) $(3, 1, \xi)$ and calculated spin wave dispersion along (c) $(2, \xi, -2)$ and (d) $(3, 1, \xi)$. The phonon mode with double periodicity was not included in our model. Black pixels show regions where no data were collected.

energies and increases dramatically with energy. The change from $L = -3$ to $L = -2$ changes the reciprocal lattice points from Q type, $(h, k, l) = (\text{even}, \text{odd}, \text{odd})$, to O type, $(h, k, l) = (\text{even}, \text{even}, \text{even})$ [10].

Figures 4(b) and 4(d) show the calculated and observed spin wave dispersion along $(3, 1, \xi)$. In this direction the intensity also approaches background at low energies and increases dramatically with energy. The change from $K = 0$ to $K = 1$ also changes the reciprocal lattice points from Q type, $(h, k, l) = (\text{odd}, \text{even}, \text{odd})$, to O type, $(h, k, l) = (\text{odd}, \text{odd}, \text{even})$.

An additional phonon mode is observed below 25 meV with twice the periodicity of the spin wave. The change in periodicity can be explained by the different unit cells corresponding to the crystallographic and magnetic structures. Ignoring small distortions of the yttrium and oxygen atoms from their ideal positions, treating the two iron sublattices as inequivalent atoms doubles the length of the unit cell along c . Views of the powder average show nondispersive modes at 15, 32, and 82 meV. The intensity of the 15 and 32 meV modes increases with higher Q , suggesting phonon excitations. The 82-meV mode was only measured over a very narrow range in Q that was insufficient to identify its Q dependence.

V. CONCLUSION

In conclusion, the inelastic spin wave spectrum was measured in the rare-earth orthoferrite YFeO₃ and analyzed with a quantitative model considering contributions from both the weak ferromagnetic and antiferromagnetic orders present in the full four-sublattice model. Excellent fits were obtained that agree well with most observed energies and intensities at both high and low energies. In addition, we observe weak magnetic scattering associated with the weak antiferromagnetic order along b . Future work will explore changes in the spin wave spectrum with spin reorientation as well as materials where the rare earth also contains magnetic interactions.

ACKNOWLEDGMENTS

We would like to acknowledge helpful conversations with Jason Haraldsen. S.E.H. and R.S.F. acknowledge support by the Laboratory's Director's fund, Oak Ridge National Laboratory. Research at Oak Ridge National Laboratory's Spallation Neutron Source was supported by the Scientific User Facilities Division, Office of Basic Energy Sciences, US Department of Energy.

APPENDIX A: SYMMETRY ANALYSIS

The magnetic symmetry of the rare-earth orthoferrites is described by linear combinations of the spins on four sublattices. The linear combination $G_{x_i} = -\vec{M}_1 + \vec{M}_2 - \vec{M}_3 + \vec{M}_4$ describes the primary G -type antiferromagnetic ordering, $F_{x_i} = \vec{M}_1 + \vec{M}_2 + \vec{M}_3 + \vec{M}_4$ describes the weak ferromagnetism, and $A_{x_i} = -\vec{M}_1 + \vec{M}_2 + \vec{M}_3 - \vec{M}_4$ describes the weak antiferromagnetism. The subscript x_i gives the direction of these vector quantities. In YFeO₃, the G -type antiferromagnetic

ordering is along a , the weak ferromagnetism is along c , and the weak antiferromagnetism is along b .

APPENDIX B: RESOLUTION CONVOLUTION

For direct comparison to experimental intensities, the effects of the magnetic form factor and the instrumental resolution were included in the calculation. The total intensity is given by

$$I(Q_0, \omega_0) = \iint F_Q^2 S(Q, \omega) R(Q - Q_0, \omega - \omega_0) dQ d\omega, \quad (\text{B1})$$

where $Q = q + G$ differs by the reciprocal lattice vector G and may be outside the first Brillouin zone. The Fe³⁺ magnetic form factor results in a lower intensity at higher values of Q and can be approximated as $F_Q = j_0(Q)$, where $j_0(Q) = A_0 e^{-a_0 s^2} + B_0 e^{-b_0 s^2} + C_0 e^{-c_0 s^2} + D_0$ and $s = \sin\theta/\lambda = Q/(4\pi)$. The coefficients are $A_0 = 0.3972$ ($a_0 = 13.2442$), $B_0 = 0.6295$ ($b_0 = 4.9034$), $C_0 = -0.0314$ ($c_0 = 0.3496$), and $D_0 = 0.0044$ from Ref. [25].

The experiment resolution shape was approximated by a Gaussian encapsulating a simulated resolution volume. For various points along the dispersion, the resolution was calculated using a full model of the incident beam line of SEQUOIA [15,16] followed by a second model that consists of the Resolution Sample and Resolution Monitor components. Both simulations were performed using the MCSTAS [26] Monte Carlo package. First, 36×10^{10} neutron packets were propagated down the incident beamline simulation. Neutron packets that succeeded in making it to the sample position were stored for later use in the secondary spectrometer simulation. Next, for each desired value of Q all of the stored neutrons from the upstream simulation were sent through the downstream simulation. The results from this second simulation provides a probability function of t and detector pixel that is transformed to ω and Q based on the kinematics of the measurement and the orientation of the crystal [27] for several points along the dispersion. The projections of these ellipsoids were taken for planes of the data and a two-dimensional Gaussian was fit around the 50% level of the observed projection of the distribution.

In two dimensions the Gaussian function is proportional to $f(x) = \exp(-\zeta^T A \zeta)$, where $\zeta = (\frac{Q}{\omega})$ and $A = (\begin{smallmatrix} a & b \\ b & c \end{smallmatrix})$. For cuts along K , the constants describing the Gaussian were $a = 1109.0 \text{ rlu}^{-2}$, $b = 0.0 (\text{rlu} \cdot \text{meV})^{-1}$, and $c = 0.48 \text{ meV}^{-2}$. For cuts along L , the constants describing the Gaussian were $a = 579.7 \text{ rlu}^{-2}$, $b = -20.0 (\text{rlu} \cdot \text{meV})^{-1}$, and $c = 1.3 \text{ meV}^{-2}$. This result was then convoluted with the model.

During the data reduction and analysis, the measured spin wave dispersion is binned and integrated over two directions and the remaining two directions plotted with the intensity given by the pixel color. To simulate this step, we integrated the calculated intensity over a volume of length $\pm 0.2 \text{ rlu}$ in the integrated directions and 0.05 rlu (representing the bin size) in the remaining direction.

[1] A. V. Kimel, A. Kirilyuk, A. Tsvetkov, R. V. Pisarev, and T. Rasing, *Nature (London)* **429**, 850 (2004).

[2] W. Eerenstein, N. D. Mathur, and J. F. Scott, *Nature (London)* **442**, 759 (2006).

- [3] Y. Tokunaga, N. Furukawa, H. Sakai, Y. Taguchi, T. Arima, and Y. Tokura, *Nat. Mater.* **8**, 558 (2009).
- [4] I. Dzyaloshinsky, *J. Phys. Chem. Solids* **4**, 241 (1958).
- [5] T. Moriya, *Phys. Rev.* **120**, 91 (1960).
- [6] R. L. White, *J. Appl. Phys.* **40**, 1061 (1969).
- [7] Y. B. Bazaliy, L. T. Tsybal, G. N. Kakazei, V. I. Kamenev, and P. E. Wigen, *Phys. Rev. B* **72**, 174403 (2005).
- [8] L. T. Tsybal, V. I. Kamenev, Y. B. Bazaliy, D. A. Khara, and P. E. Wigen, *Phys. Rev. B* **72**, 052413 (2005).
- [9] V. P. Plakhty, Y. P. Chernenkov, and M. N. Bedrizova, *Solid State Commun.* **47**, 309 (1983).
- [10] S. M. Shapiro, J. D. Axe, and J. P. Remeika, *Phys. Rev. B* **10**, 2014 (1974).
- [11] S. Artyukhin, M. Mostovoy, N. P. Jensen, D. Le, K. Prokes, V. G. de Paula, H. N. Bordallo, A. Maljuk, S. Landsgesell, H. Ryll, B. Klemke, S. Paeckel, K. Kiefer, K. Lefmann, L. T. Kuhn, and D. N. Argyriou, *Nat. Mater.* **11**, 694 (2012).
- [12] A. Gukasov, U. Steigenberger, S. Barilo, and S. Guretskii, *Phys. B: Condens. Matter* **234–236**, 760 (1997), Proceedings of the First European Conference on Neutron Scattering.
- [13] R. M. White, R. J. Nemanich, and C. Herring, *Phys. Rev. B* **25**, 1822 (1982).
- [14] G. Ehlers, A. A. Podlesnyak, J. L. Niedziela, E. B. Iverson, and P. E. Sokol, *Rev. Sci. Instrum.* **82**, 085108 (2011).
- [15] G. E. Granroth, D. H. Vandergriff, and S. E. Nagler, *Phys. B: Condens. Matter* **385–86**, 1104 (2006).
- [16] G. E. Granroth, A. I. Kolesnikov, T. E. Sherline, J. P. Clancy, K. A. Ross, J. P. C. Ruff, B. D. Gaulin, and S. E. Nagler, *J. Phys.: Conf. Ser.* **251**, 012058 (2010).
- [17] <http://www.mantidproject.org>
- [18] R. Azuah, L. Kneller, Y. Qiu, P. Tregenna-Piggott, C. Brown, J. Copley, and R. Dimeo, *J. Res. Natl. Inst. Stan. Technol.* **114**, 341 (2009).
- [19] G. Shirane, S. Shapiro, and J. Tanquada, *Neutron Scattering with a Triple-Axis Spectrometer* (Cambridge University Press, Cambridge, England, 2004).
- [20] J. T. Haraldsen and R. S. Fishman, *J. Phys.: Condens. Matter* **21**, 216001 (2009).
- [21] R. S. Fishman, J. T. Haraldsen, N. Furukawa, and S. Miyahara, *Phys. Rev. B* **87**, 134416 (2013).
- [22] S. G. Johnson, “The NLOPT nonlinear-optimization package”, <http://ab-initio.mit.edu/nlopt>
- [23] G. F. Herrmann, *Phys. Rev.* **133**, A1334 (1964).
- [24] N. Koshizuka and K. Hayashi, *J. Phys. Soc. Jpn.* **57**, 4418 (1988).
- [25] A. J. Dianoux and G. Lander, *Neutron Data Booklet* (OCP Science, Philadelphia, 2003).
- [26] K. Lefmann and K. Nielsen, *Neutron News* **10**, 20 (1999).
- [27] M. D. Lumsden, J. Robertson, and M. Yethiraj, *J. Appl. Cryst.* **38**, 405 (2005).